Charge Versus Energy Transfer in Atomically Thin Graphene-Transition Metal Dichalcogenide van der Waals Heterostructures

Guillaume Froehlicher,[*] Etienne Lorchat, and Stéphane Berciaud[†]

Université de Strasbourg, CNRS, Institut de Physique et Chimie des Matériaux de Strasbourg (IPCMS), UMR 7504, F-67000 Strasbourg, France

(Received 1 August 2017; revised manuscript received 1 December 2017; published 18 January 2018; corrected 9 March 2018)

Made from stacks of two-dimensional materials, van der Waals heterostructures exhibit unique light-matter interactions and are promising for novel optoelectronic devices. The performance of such devices is governed by near-field coupling through, e.g., interlayer charge and/or energy transfer. New concepts and experimental methodologies are needed to properly describe two-dimensional heterointerfaces. Here, we report an original study of interlayer charge and energy transfer in atomically thin metal-semiconductor [i.e., graphene-transition metal dichalcogenide (TMD, here molybdenum diselenide, $MoSe_2$)] heterostructures using a combination of microphotoluminescence and Raman scattering spectroscopies. The photoluminescence intensity in graphene/$MoSe_2$ is quenched by more than 2 orders of magnitude and rises linearly with the incident photon flux, demonstrating a drastically shortened (about 1 ps) room-temperature $MoSe_2$ exciton lifetime. Key complementary insights are provided from a comprehensive analysis of the graphene and $MoSe_2$ Raman modes, which reveals net photoinduced electron transfer from $MoSe_2$ to graphene and hole accumulation in $MoSe_2$. Remarkably, the steady-state Fermi energy of graphene saturates at 290 ± 15 meV above the Dirac point. This reproducible behavior is observed both in ambient air and in vacuum and is discussed in terms of intrinsic factors (i.e., band offsets) and environmental effects. In this saturation regime, balanced photoinduced flows of electrons and holes may transfer to graphene, a mechanism that effectively leads to energy transfer. Using a broad range of incident photon fluxes and diverse environmental conditions, we find that the presence of net photoinduced charge transfer has no measurable impact on the near-unity photoluminescence quenching efficiency in graphene/$MoSe_2$. This absence of correlation strongly suggests that energy transfer to graphene (either in the form of electron exchange or dipole-dipole interaction) is the dominant interlayer coupling mechanism between atomically thin TMDs and graphene.

DOI: 10.1103/PhysRevX.8.011007

Subject Areas: Condensed Matter Physics, Materials Science, Optics

I. INTRODUCTION

Charge and energy transfer (CT, ET) play a prominent role in atomic, molecular, and nanoscale systems. On the one hand, Förtser-type energy transfer [1], mediated by relatively long-range (up to several nm) near-field dipole-dipole coupling, is an essential step in photosynthesis [2] and is now engineered in a variety of light-harvesting devices and distance sensors [3,4]. Charge transfer, on the other hand, is a much shorter-range process (about 1 nm) that plays a key role in a number of molecular and solid-state systems and is at the origin of the operation of photodetectors and solar cells [5,6]. In the limit of orbital overlap between donor and acceptor systems, electron exchange, resulting in no net charge transfer and also known as Dexter-type energy transfer [7], may occur. The efficiencies of CT and ET depend very sensitively on the donor-acceptor distance, on the energy-level (or bands) offsets, and on the local dielectric and electrostatic environment. CT and ET processes may have beneficial or detrimental impact on the performance of optoelectronic devices and therefore deserve fundamental investigations.

In this context, two-dimensional materials [2DM—such as graphene (Gr), boron nitride, transition metal dichalcogenides (TMDs), black phosphorus,…] provide an extraordinary toolkit to investigate novel regimes of CT and ET. Indeed, the very diverse and complementary physical properties of 2DM can be tailored and controlled at the single-layer level but also combined and possibly enhanced within so-called van der Waals heterostructures (vdWHs) [8–10]. The vdWHs provide a new paradigm of

[*]Present address: Department of Physics, University of Basel, Klingelbergstrasse 82, CH-4056 Basel, Switzerland.

[†]stephane.berciaud@ipcms.unistra.fr

clean, ultra-smooth, two-dimensional heterointerfaces [11]. Since their van der Waals gap is only of a few Å, band bending and depletion regions cannot develop in vdWH. As a result, well-established concepts borrowed from the physics of bulk or low-dimensional heterojunctions [6] must be adapted with great care when describing the optoelectronic response of vdWHs. In addition, the ultimate proximity between the atomically thin building blocks that compose a vdWH potentially allows ultra-efficient CT and/or ET.

Among the vast library of 2DM, graphene [12] and atomically thin semiconducting TMDs (with formula MX_2, with M = Mo, W and X = S, Se, Te) [10,13,14] have attracted particular interest for optoelectronic applications [15–25]. Indeed, graphene may act as a highly tunable transparent electrode, endowed with exceptional physical properties [26–28], while monolayer TMDs are direct band-gap semiconductors with unusually strong light-matter interactions and excitonic effects [10,29,30], as well as unique spin, valley, and optoelectronic properties [10,30,31]. Photodetectors based on graphene and TMDs display high photoresponsivity and photogain [15–19], down to picosecond time scales [20]. The photophysics of Gr/TMD vdWHs is governed by near-field interlayer CT and/or ET (ICT, IET). In the related and most-studied case of TMD/TMD heterojunctions with type-II band alignment, subpicosecond ICT and subsequent interlayer exciton formation is thought to be the dominant coupling mechanism [31–36]. However, recent photoluminescence excitation spectroscopy studies in $MoSe_2/WS_2$ vdWH have suggested that IET may be at least as efficient as ICT [37].

In contrast, fundamental studies of IET and ICT remain scarce in Gr/TMD vdWH. Photoinduced ICT has been observed in Gr/MoS_2 photodetectors [18]. Recent transient absorption studies have evidenced fast interlayer coupling in Gr/WS_2 vdWHs and tentatively assigned it to photoinduced ICT [24]. Yet, such studies were mostly performed under ambient conditions, and the environmental effects need to be assessed. Importantly, in Ref. [20], the internal quantum efficiency of Gr/TMD photodetectors degrades when the active TMD layer is thinned down to the monolayer limit, possibly due to efficient IET to graphene. Overall, IET has been surprisingly overlooked in vdWH, whereas related studies in hybrid heterostructures composed of nanoscale emitters (molecules, quantum dots, quantum wells,…) interfaced with carbon nanotubes [38], graphene [39–42], and TMDs [43,44] have consistently demonstrated highly efficient Förster-type ET.

Unraveling the relative efficiencies of ICT and IET in vdWH is a timely challenge for optoelectronics. For this purpose, optical spectroscopy offers minimally invasive and spatially resolved tools. First exciton dynamics and interlayer coupling can be probed with great sensitivity using microphotoluminescence (PL) spectroscopy [10,31]. Second, micro-Raman scattering spectroscopy allows quantitative measurements of doping and CT, as it has been demonstrated in graphene [45–49] and in MoS_2 [50,51] but not yet in vdWHs.

In this paper, using an original combination of PL and Raman spectroscopies, we are able to disentangle contributions from ICT and IET in model vdWHs made of single-layer graphene stacked onto single-layer molybdenum diselenide ($MoSe_2$) (hereafter denoted $Gr/MoSe_2$) in the absence of any externally applied electric field. While highly efficient exciton-exciton annihilation and subsequent saturation of the PL intensity is, as expected, observed in bare $MoSe_2$ as the incident photon flux is increased, the PL in $Gr/MoSe_2$ is massively quenched, and its intensity rises linearly with the incident photon flux, demonstrating a drastically shortened room-temperature exciton lifetime in $MoSe_2$. Key complementary insights are provided from a comprehensive analysis of the graphene and $MoSe_2$ Raman modes, which reveals net photoinduced electron transfer from $MoSe_2$ to graphene and hole accumulation in $MoSe_2$. Remarkably, the steady-state Fermi energy of graphene saturates at 290 ± 15 meV above the Dirac point. In this saturation regime, balanced flows of electrons and holes transfer to graphene, resulting in no net photoinduced charge transfer. This reproducible behavior is observed both in ambient air and in vacuum and is discussed in terms of intrinsic factors (i.e., band offsets) and extrinsic effects associated with native doping and charge trapping. Using a broad range of incident photon fluxes and diverse environmental conditions, we find that the existence of net photoinduced charge transfer has no measurable impact on the near-unity photoluminescence quenching efficiency in $graphene/MoSe_2$. This absence of correlation strongly suggests that energy transfer to graphene (either in the form of Dexter or Förster processes) is the dominant interlayer coupling mechanism between atomically thin TMDs and graphene. Our results provide a better understanding of the atomically thin, two-dimensional, metal-semiconductor (i.e., Schottky) junction, a ubiquitous building block in emerging optoelectronic devices, and will serve as a guide to engineer charge-carrier and exciton transport in two-dimensional materials.

II. CHARACTERIZATION OF THE $Gr/MoSe_2$ HETEROSTRUCTURE

Figure 1(a) shows an optical image of a $Gr/MoSe_2$ vdWH (sample S_1) deposited onto a Si/SiO_2 substrate (see Appendix for details on sample fabrication). From AFM measurements (see Ref. [52], Fig. S1), we can distinguish a region of the heterostructure [highlighted with a white dashed contour in Fig. 1(a)], where the two layers are well coupled, as evidenced by the small surface roughness [9] and the small height difference of approximately 0.65 nm between the surface of $MoSe_2$ and Gr [see Fig. 1(b)]. Outside this region, the interface shows submicrometer size "pockets" and an average step of about 2–3 nm [see Fig. 1(b)] between $MoSe_2$ and Gr. Hereafter, these two regions are

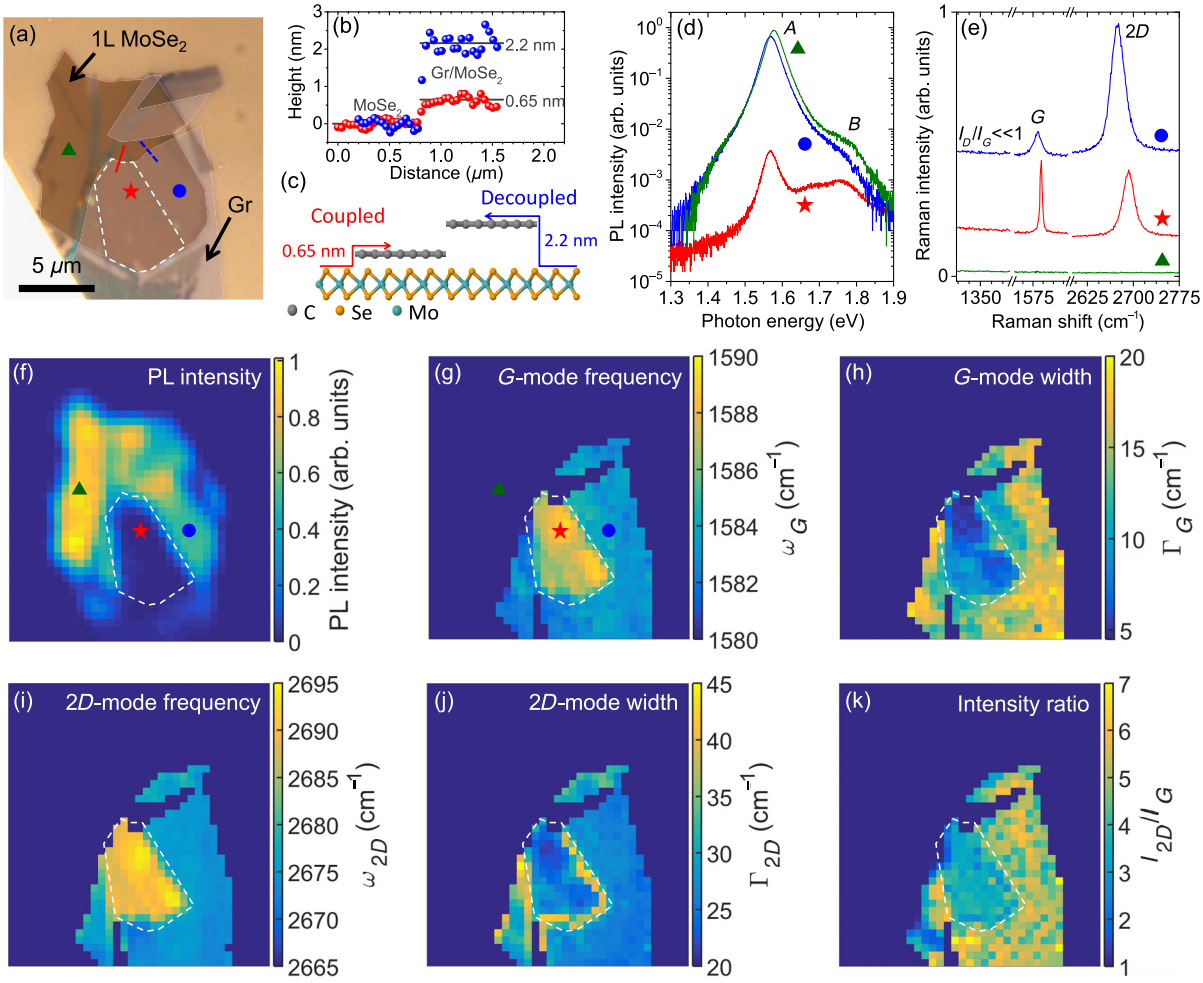

FIG. 1. (a) Optical image of a single-layer graphene/single-layer $MoSe_2$ van der Waals heterostructure deposited onto a Si/SiO_2 substrate (sample S_1). The coupled part of the heterostructure is represented by the white dashed contour. (b) Height profiles, measured by atomic force microscopy, along the dashed blue and red lines drawn in panel (a). (c) Schematic of the heterostructure showing the coupled and decoupled regions. Photoluminescence (d) and Raman scattering (e) spectra recorded on the three spots shown in panels (f) and (g), respectively. In panels (d) and (e), the spectra are plotted with the same color as the symbols in panels (f) and (g), respectively. (f) $MoSe_2$ photoluminescence intensity map. (g)–(k) Hyperspectral Raman maps of the (g) G-mode frequency ω_G, (h) G-mode FWHM Γ_G, (i) $2D$-mode frequency ω_{2D}, (j) $2D$-mode FWHM Γ_{2D}, and (k) ratio between the integrated intensities of the $2D$- and G-mode features (I_{2D}/I_G) measured on single-layer graphene. All maps have the same scale as in panel (a) and were recorded in ambient air at a laser photon energy of 2.33 eV, with an incident photon flux $\Phi_{ph} = 2 \times 10^{19}$ cm^{-2} s^{-1} and $\Phi_{ph} = 2 \times 10^{22}$ cm^{-2} s^{-1} for photoluminescence and Raman measurements, respectively.

referred to as coupled and decoupled $Gr/MoSe_2$, respectively [see Fig. 1(c) and Ref. [52], Fig. S1].

Typical photoluminescence (PL) and Raman spectra from three different points of the sample are shown in Figs. 1(d) and 1(e), respectively. Unless otherwise noted, the samples were optically excited in the continuous-wave regime using a single longitudinal-mode, linearly polarized laser at a photon energy of 2.33 eV, well above the optical band gap of $MoSe_2$.

Figures 1(f)–1(k) display the hyperspectral maps of (f) the $MoSe_2$ PL intensity, (g)–(j) the frequencies ($\omega_{G,2D}$) and full widths at half maximum (FWHM, $\Gamma_{G,2D}$) of the Raman G- and $2D$-mode features [53], and (k) the ratio of their integrated intensities (I_{2D}/I_G). Note that no defect-induced D-mode feature [53] (expected around 1350 cm^{-1}) emerges from the background [see Fig. 1(e)], showing the very good quality of our sample. All hyperspectral maps allow us to distinctively identify the coupled and decoupled $Gr/MoSe_2$ regions and confirm the trends observed on selected points.

The PL spectra in Fig. 1(d) are characteristic of single-layer $MoSe_2$, with the A and B excitons [54] near 1.57 eV and 1.75 eV, respectively. Remarkably, the $MoSe_2$ PL intensity is about 300 times smaller on coupled $Gr/MoSe_2$ than on $MoSe_2/SiO_2$, while it is only reduced by a modest factor of approximately 2 on decoupled $Gr/MoSe_2$ [Figs. 1(d) and 1(f)]. Such massive PL quenching, also observed for other Gr/TMD vdWHs [20,24], demonstrates strong interlayer coupling and suggests a much-reduced exciton lifetime.

As shown in Figs. 1(e) and 1(g)–1(k), interlayer coupling also dramatically affects the Raman response of graphene. Indeed, on coupled Gr/$MoSe_2$, the G-mode feature upshifts and becomes narrower, and the I_{2D}/I_G ratio decreases [Fig. 1(k)] with respect to reference measurements on the neighboring pristine graphene deposited on SiO_2 (Gr/SiO_2) and decoupled Gr/$MoSe_2$ regions [Figs. 1(e) and 1(k)]. These observations are robust evidence of an increased charge carrier concentration in graphene [47,48]. Surprisingly, we observe an upshift of the 2D-mode frequency on coupled Gr/$MoSe_2$ [Fig. 1(i)], which is too high to be solely induced by doping or strain [48,55,56] and seems qualitatively similar to previous reports on graphene deposited on thick boron nitride terraces [57,58] and monolayer MoS_2 grown on graphene [21]. Possible origins for this upshift are discussed in Ref. [52] (Fig. S15).

In the following sections, we quantitatively investigate exciton dynamics (Sec. III) and interlayer charge transfer (Sec. IV).

III. EXCITON DYNAMICS IN Gr/$MoSe_2$

Although PL quenching has been reported in previous studies of Gr/TMD heterostructures (see Fig. 1 in Ref. [59] and Supplementary Fig. 6 in Ref. [20]), quantitative analysis of PL quenching and its interpretation in terms of IET and ICT have not been reported thus far.

Figures 2(a) and 2(b) display the normalized PL spectra of $MoSe_2$ recorded on $MoSe_2/SiO_2$, and decoupled and

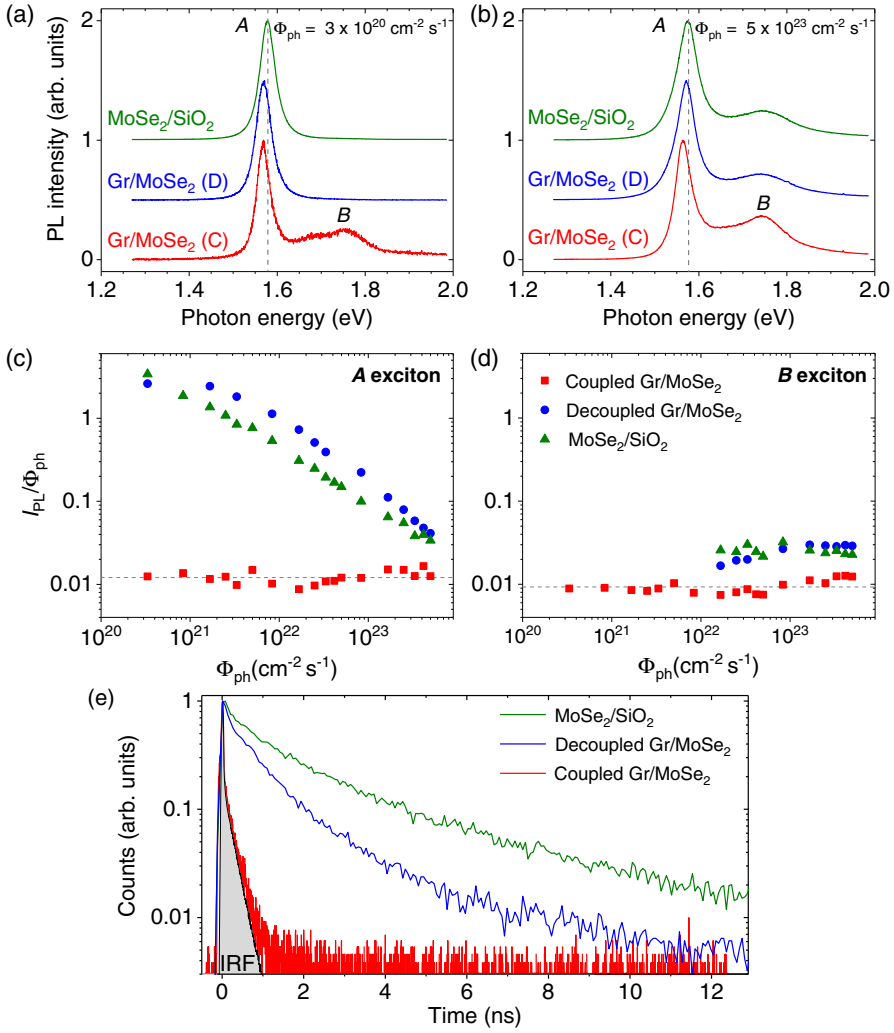

FIG. 2. Normalized photoluminescence spectra of $MoSe_2$ recorded in the cw regime at a laser photon energy of 2.33 eV, with an incident photon flux (a) $\Phi_{ph} = 3 \times 10^{20}$ cm^{-2} s^{-1} and (b) $\Phi_{ph} = 5 \times 10^{23}$ cm^{-2} s^{-1} for $MoSe_2/SiO_2$, and decoupled (D) and coupled (C) Gr/$MoSe_2$. The A and B excitons are labeled, and the position of the A exciton in $MoSe_2/SiO_2$ is indicated by a gray vertical dashed line. (b) Integrated photoluminescence intensity of the (c) A and (d) B exciton normalized by Φ_{ph} as a function of Φ_{ph}. The gray dashed line is a guide to the eye. The error bars are smaller than the symbol size. (e) Photoluminescence decays recorded using a pulsed laser at 1.96 eV with a fluence of 2.2×10^{11} cm^{-2} per pulse. The gray area corresponds to the instrument response function (IRF). All measurements were performed in ambient air.

coupled Gr/$MoSe_2$ at low- and high-incident photon flux Φ_{ph}. The *A* exciton PL feature of coupled Gr/$MoSe_2$/SiO_2 is marginally redshifted (by ≈ 10 meV) with respect to that of air/$MoSe_2$/SiO_2, irrespective of Φ_{ph}. Considering the drastically different dielectric environments, such a surprisingly small reduction of the *optical* band gap is assigned to the near-perfect compensation of the reductions of the electronic band gap and exciton binding energy in graphene-capped $MoSe_2$ [60–62]. The line shapes of the *A*-exciton features are quite similar, except for a small but reproducible narrowing of the *A*-exciton linewidth in coupled Gr/$MoSe_2$. Similar narrowing has recently been observed in TMD layers fully encapsulated in boron nitride [63,64] and likely results from a reduction of inhomogeneous broadening and pure dephasing in graphene-capped TMD samples.

The integrated PL intensities of the *A* and *B*-exciton features (denoted $I_{PL}^{A,B}$) normalized by Φ_{ph} are plotted as a function of Φ_{ph} in Figs. 2(c) and 2(d), respectively. For $MoSe_2$/SiO_2 and decoupled Gr/$MoSe_2$, I_{PL}^{A}/Φ_{ph} drops abruptly as Φ_{ph} is increased. This effect stems from highly efficient exciton-exciton annihilation (EEA), as previously evidenced in TMD monolayers [65,66]. In the case of coupled Gr/$MoSe_2$, I_{PL}^{A}/Φ_{ph} remains constant, within experimental accuracy, up to $\Phi_{ph} \sim 10^{24}$ cm^{-2} s^{-1}. As a result, while I_{PL}^{A} is about 300 times weaker on coupled Gr/$MoSe_2$ than on bare $MoSe_2$ at $\Phi_{ph} = 3 \times 10^{20}$ cm^{-2} s^{-1}, this quenching factor reduces down to about 3 at $\Phi_{ph} = 6 \times 10^{23}$ cm^{-2} s^{-1}. Strong PL quenching, together with the linear scaling of I_{PL}^{A} with Φ_{ph}, demonstrates that interlayer coupling between graphene and $MoSe_2$ opens up a nonradiative decay channel for *A* excitons, which dramatically reduces the *A*-exciton lifetime and is sufficiently fast to bypass EEA. Very similar PL quenching and exciton dynamics have been observed in other Gr/$MoSe_2$/SiO_2 samples (see Ref. [52], Figs. S11–S13) as well as in Gr/WS_2/SiO_2 (see Ref. [52], Fig. S14) and Gr/WSe_2/SiO_2 (data not shown). The shortening of the *A*-exciton lifetime is further substantiated by the analysis of the *hot* luminescence from the *B* exciton (note that our samples are photoexcited at 2.33 eV, i.e., well above the *B* exciton in $MoSe_2$). In bare $MoSe_2$ and decoupled Gr/$MoSe_2$, $I_{PL}^{A} \gg I_{PL}^{B}$, whereas $I_{PL}^{B} \sim I_{PL}^{A}$ in coupled Gr/$MoSe_2$. Interestingly, I_{PL}^{B} is very similar in the three cases and scales linearly with Φ_{ph} [see Fig. 2(d)]. These observations suggest (i) that interlayer coupling does not significantly affect exciton formation and exciton decay until a population of *A* excitons is formed, and (ii) that the *A*-exciton lifetime in Gr/$MoSe_2$ is not appreciably longer than the $B \rightarrow A$ decay time. The latter is typically in the subpicosecond range [67] in atomically thin TMDs and provides a lower bound for the *A*-exciton lifetime in Gr/$MoSe_2$. Additional insights are provided by time-resolved photoluminescence measurements recorded in ambient conditions [see Fig. 2(e)]. Bare $MoSe_2$ and decoupled Gr/$MoSe_2$ display nonmonoexponential decays [68] with average exciton lifetime of about 1 ns. As anticipated, the PL decay of Gr/$MoSe_2$ is too fast to be resolved using our experimental apparatus, confirming that the *A*-exciton lifetime is significantly shorter than our time resolution of approximately 20 ps. Using the estimated decay time of bare $MoSe_2$ and a typical quenching factor of 300 (i.e., a quenching efficiency of 99.7%) in the low fluence limit, we can assume a conservative upper bound of a few ps for the exciton lifetime in coupled Gr/$MoSe_2$.

IV. INTERLAYER CHARGE TRANSFER

A. Net photoinduced electron transfer to graphene

The fast $MoSe_2$ exciton decay in Gr/$MoSe_2$ heterostructures may arise from a combination of ICT and IET processes. In this section, we introduce an original Raman-based readout of the steady-state charge carrier density in both materials.

Figure 3 shows the evolution of $\omega_{G,2D}$, $\Gamma_{G,2D}$, and I_{2D}/I_G measured in sample S_1 as a function of Φ_{ph} in ambient air. The corresponding spectra are shown in Ref. [52] (Fig. S2). First, for Gr/SiO_2 and decoupled Gr/$MoSe_2$, $\omega_G \approx 1583$ cm^{-1}, $\Gamma_G \approx 16$ cm^{-1}, $\omega_{2D} \approx 2674$ cm^{-1}, and $I_{2D}/I_G \approx 6.5$ do not show any appreciable variation as Φ_{ph} augments. These values correspond to very weakly doped graphene ($|n_{Gr}| \sim 10^{11}$ cm^{-2} or $|E_F^{Gr}| \lesssim 100$ meV) [47,48,69]. In addition, the absence of measurable phonon softening at high Φ_{ph} indicates that the laser-induced temperature rise remains below about 100 K [70].

Second, for coupled Gr/$MoSe_2$, ω_G distinctly rises as Φ_{ph} is increased, whereas Γ_G decreases [see Figs. 3(a)–3(c)]. Additionally, I_{2D}/I_G [Fig. 3(d)] drops significantly. These spectroscopic features provide strong evidence for net photoinduced ICT from $MoSe_2$ to graphene [47,48]. We can now identify the sign of the net transferred charge flow using the correlation between ω_{2D} and ω_G in Fig. 3(e) as in Refs. [48,55]. As Φ_{ph} is increased, the data for Gr/SiO_2 and decoupled Gr/$MoSe_2$ show no clear correlations. In contrast, on coupled Gr/$MoSe_2$, ω_{2D} and ω_G display a linear correlation with a slope of approximately 0.11, a value that clearly points towards photoinduced electron doping in graphene [48].

Using well-established theoretical modeling of electron-phonon coupling in doped graphene [46,71], we quantitatively determine the Fermi energy of graphene relative to the Dirac point E_F^{Gr} or, equivalently, its doping level n_{Gr}. The values of E_F^{Gr} and n_{Gr} extracted from a global fitting procedure (see Ref. [48]) are plotted in Fig. 3(f). As further discussed in Sec. V, E_F^{Gr} (n_{Gr}) saturates as Φ_{ph} is increased and reaches up to approximately 280 meV ($\approx 5 \times 10^{12}$ cm^{-2}).

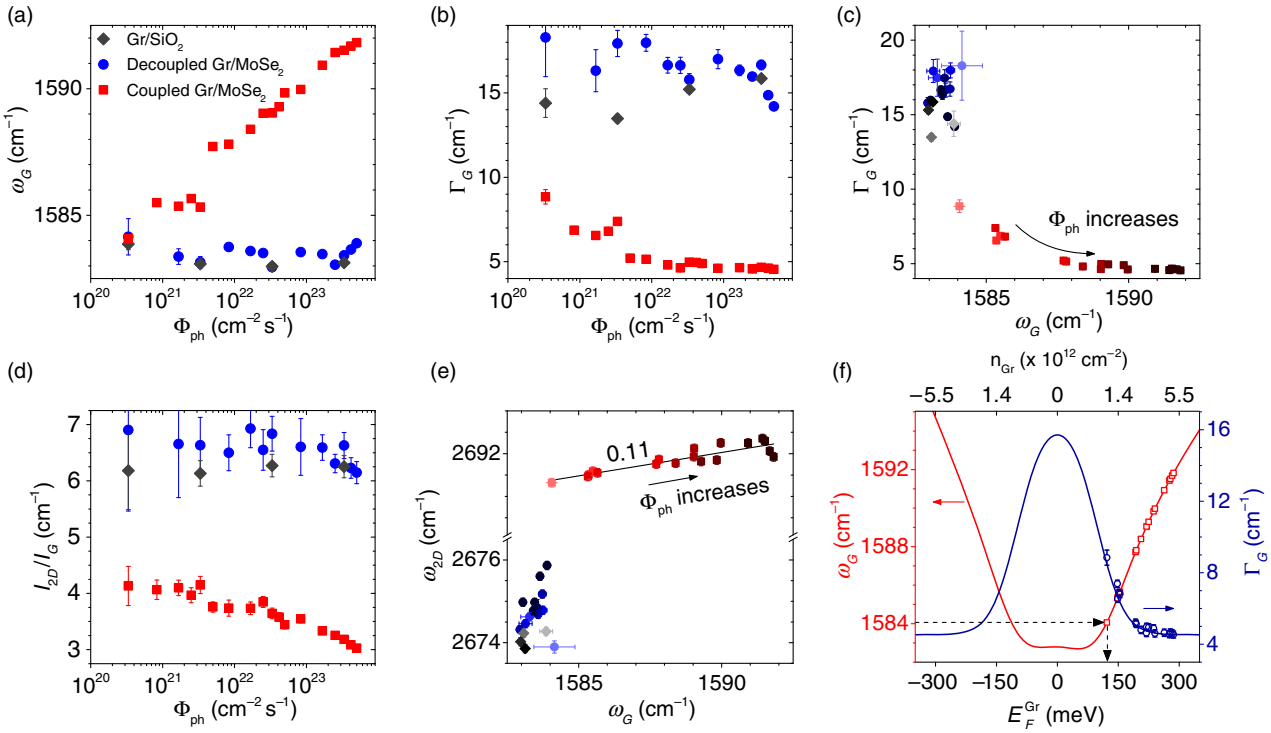

FIG. 3. (a) Raman G-mode frequency ω_G and (b) full width at half maximum Γ_G recorded at a laser photon energy of 2.33 eV as a function of the incident photon flux Φ_{ph} for coupled (red squares) and decoupled (blue circles) $Gr/MoSe_2$ and for Gr/SiO_2 (gray diamonds) (see Fig. 1). (c) Correlation between Γ_G and ω_G under increasing Φ_{ph}. (d) Ratio between the integrated intensity of the 2D-mode feature and that of the G-mode feature I_{2D}/I_G as a function of Φ_{ph}. (e) Correlation between ω_{2D} and ω_G under increasing Φ_{ph}. The color of the symbols in panels (c) and (e) gets darker with increasing Φ_{ph}. (f) ω_G (red squares, left axis) and Γ_G (blue circles, right axis) as a function of the graphene Fermi energy E_F^{Gr} and doping level n_{Gr}. The solid lines are theoretical calculations [46,48]. All measurements were performed in ambient air.

B. Hole accumulation in $MoSe_2$

Net electron transfer to graphene naturally implies hole accumulation in $MoSe_2$. Depending on the initial doping of $MoSe_2$, photoinduced hole accumulation in $MoSe_2$ should allow or impede the formation of charged excitons (trions). However, at room temperature, trions in $MoSe_2$ are not stable enough [72] to allow the observation of trion emission in our PL spectra. However, as in Sec. IV A, we can seek for fingerprints of ICT in the high-resolution Raman response of $MoSe_2$.

Figure 4(a) shows the $MoSe_2$ Raman spectra from $MoSe_2/SiO_2$, and decoupled and coupled $Gr/MoSe_2$. In addition to several higher-order resonant features involving finite-momentum phonons, one can identify the two Raman-active one-phonon modes in monolayer $MoSe_2$ with A_1' symmetry (near 242 cm^{-1}) and E' symmetry (near 289 cm^{-1}) [73,74]. The faint E' mode feature is slightly downshifted on coupled $Gr/MoSe_2$, as compared to $MoSe_2/SiO_2$. The prominent A_1'-mode feature is similar for $MoSe_2/SiO_2$ and decoupled $Gr/MoSe_2$, but it distinctively blueshifts (by approximately 0.5 cm^{-1}) and gets narrower (by approximately 20%) for coupled $Gr/MoSe_2$ [see Fig. 4(b)].

As in the case of graphene, changes in the Raman spectra can tentatively be assigned to doping, with possible spurious contributions from native strain, laser-induced heating, van der Waals coupling [75] and surface effects [76–78]. Interestingly, recent Raman studies in MoS_2 monolayers have demonstrated that the A_1'-mode phonon undergoes modest doping-induced phonon renormalization, namely, a downshift and a broadening for increasing electron concentration, whereas the E'-mode phonon is largely insensitive to doping [50,51]. Conversely, also in MoS_2, it was shown that under tensile (resp. compressive) strain, the E'-mode feature undergoes much larger shifts than the A_1'-mode feature [74,79]. The A_1' and E' phonons may thus be used as probes of ICT and strain, respectively. Based on these considerations, the minute E' phonon softening observed irrespective of Φ_{ph} in $Gr/MoSe_2$ relative to $MoSe_2/SiO_2$ suggests a slightly larger native tensile strain on $Gr/MoSe_2$, which has no impact whatsoever on ICT (see Ref. [52], Fig. S4–S8). More importantly, the upshifted and narrower A_1'-mode feature consistently observed up to $\Phi_{ph} \approx 6 \times 10^{23}$ cm^{-2} s^{-1} in coupled $Gr/MoSe_2$ indicates a lower electron density in $MoSe_2$ than in decoupled $Gr/MoSe_2$ and $MoSe_2/SiO_2$.

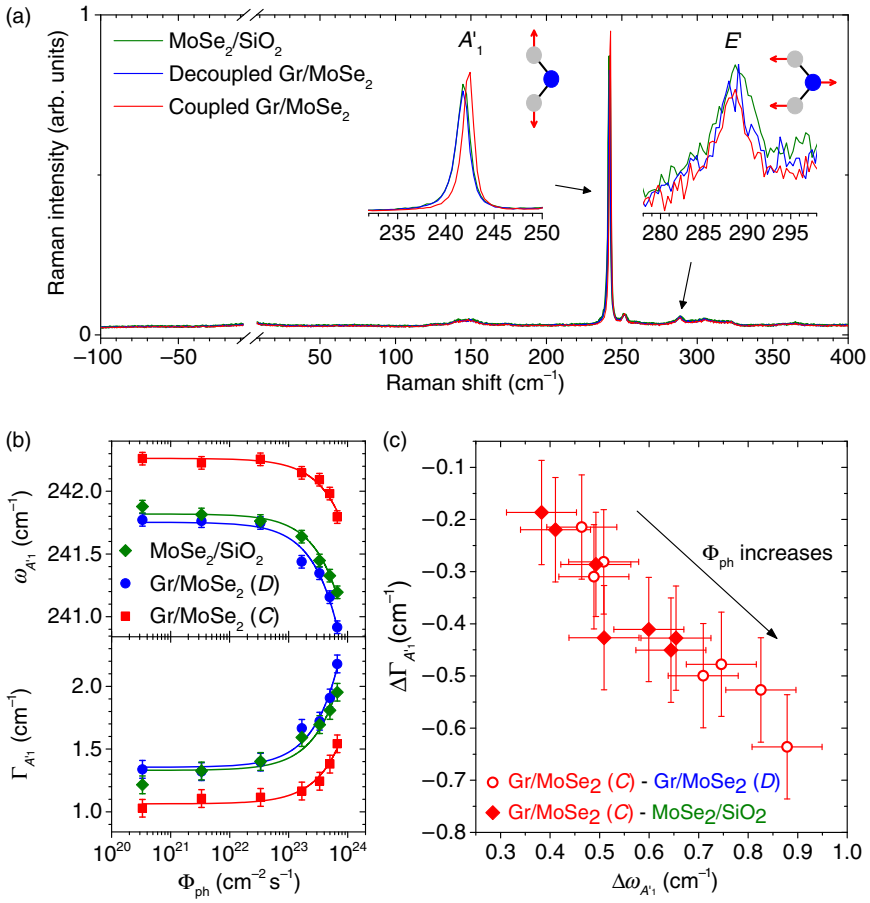

FIG. 4. (a) Raman spectra of $MoSe_2$ recorded at 2.33 eV, with $\Phi_{ph} = 3.3 \times 10^{22}$ cm^{-2} s^{-1} for $MoSe_2/SiO_2$ (green), coupled (C, in red) and decoupled (D, in blue) $Gr/MoSe_2$. The insets show a close-up of the two one-phonon Raman-active modes in single-layer $MoSe_2$, namely, the A_1' and E' modes. The corresponding atomic displacements are sketched. (b) Extracted frequency (top) and FWHM (bottom) of the A_1'-mode feature as a function of the incident photon flux Φ_{ph} for $MoSe_2/SiO_2$ (green diamonds), coupled (red squares) and decoupled (blue circles) $Gr/MoSe_2$. The solid lines are linear fits. (c) Difference between the A_1'-mode FWHMs $\Delta\Gamma_{A_1'}$ as a function of the difference between the A_1'-mode frequencies $\Delta\omega_{A_1'}$ for coupled and decoupled $Gr/MoSe_2$ (open circles), and for coupled $Gr/MoSe_2$ and $MoSe_2/SiO_2$ (filled diamonds). All measurements were performed in ambient air.

However, in the three regions of the sample, the frequency (resp. FWHM) of the A_1'-mode feature downshifts (resp. upshifts) linearly as Φ_{ph} is increased, respectively. Such trends counterintuitively suggest photoinduced electron doping in $MoSe_2$. We tentatively assign the observed evolution of the A_1'-mode feature to a slight laser-induced temperature increase (estimated below 100 K [80] at $\Phi_{ph} \approx 6 \times 10^{23}$ cm^{-2} s^{-1}), possibly combined with related photogating effects involving the presence of molecular adsorbates and trapped charges both acting as electron acceptors and laser-assisted desorption of the latter [51]. Remarkably, as shown in Fig. 4(c), the difference between the A_1' frequencies (FWHM) measured on coupled $Gr/MoSe_2$ and decoupled $Gr/MoSe_2$ or $MoSe_2/SiO_2$ monotonically increases (decreases) as Φ_{ph} is increased. These observations correspond to a net photoinduced hole doping for $MoSe_2$ in coupled $Gr/MoSe_2$, relative to decoupled $Gr/MoSe_2$ and $MoSe_2/SiO_2$, consistently with the net photoinduced electron transfer from $MoSe_2$ to graphene demonstrated in Fig. 3.

V. ENVIRONMENTAL EFFECTS

The charge density and exciton dynamics in 2D materials are known to be influenced by environmental effects, in particular, by molecular adsorbates and the underlying substrate [49,51,81,82]. To determine the generality of the results presented above, we compare, in Figs. 5(a) and 5(b), the evolution of E_F^{Gr} with increasing Φ_{ph} recorded in ambient air and under high vacuum ($\lesssim 10^{-4}$ mbar) for a set of five samples, wherein strong PL quenching has been observed (see Ref. [52], Fig. S11). Remarkably, in ambient air, all samples display (i) different initial doping at low Φ_{ph}, (ii) distinct sublinear rises of E_F^{Gr} with increasing Φ_{ph}, and (iii) similar saturation at E_F^{Gr} around 290 ± 15 meV [i.e., $n_{Gr} \approx (5 \pm 0.5) \times 10^{12}$ cm^{-2}]. Interestingly, under

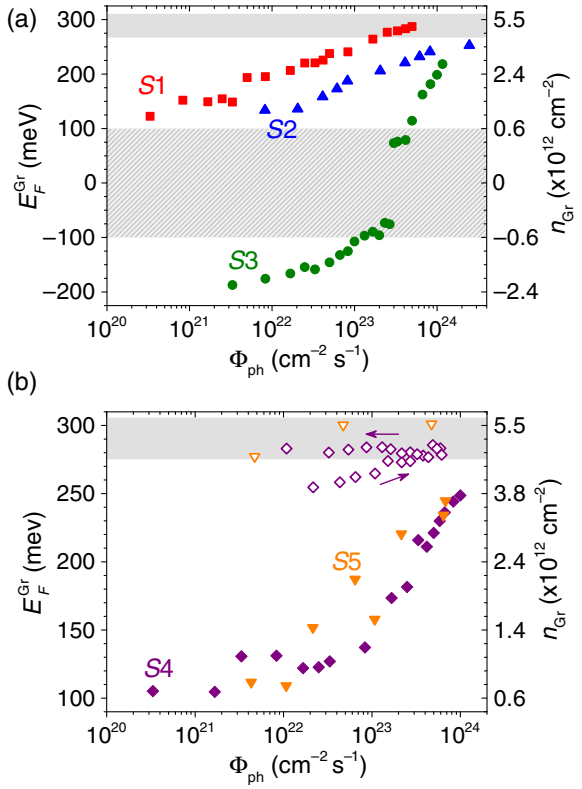

FIG. 5. (a) Fermi energy E_F^{Gr} (left) and doping level n_{Gr} (right) in graphene as a function of the incident photon flux Φ_{ph}. Measurements on three selected $Gr/MoSe_2$ samples (denoted S_1, S_2, and S_3) are represented with different symbols. The data shown in Figs. 1–4 are from S_1. The hatched region denotes the range of E_F^{Gr} close to the charge neutrality point where there is an uncertainty on the sign and on the exact value of E_F^{Gr}. The gray rectangle illustrates the saturation value of E_F^{Gr}. (b) E_F^{Gr} (left) and n_{Gr} (right) as a function of Φ_{ph} obtained under ambient conditions (filled symbols) and in vacuum (open symbols) at the same point of a $Gr/MoSe_2/SiO_2$ and a $MoSe_2/Gr/SiO_2$ heterostructure, denoted S_4 and S_5, respectively. Measurements under vacuum in S_4 are shown as Φ_{ph} is swept forward for the first time and then backward (see arrows).

vacuum, we systematically observe a transient regime with a photoinduced rise of E_F^{Gr} (at fixed Φ_{ph}) towards a saturation value that is attained on a rather long time scale (typically several minutes, depending on Φ_{ph}; see Fig. 5(b) and Ref. [52], Fig. S10). Once E_F^{Gr} has reached its saturation value, it becomes completely independent of Φ_{ph} [see Fig. 5(b)].

The distinct charge transfer dynamics observed under ambient conditions and in vacuum shed light on the role of molecular adsorbates at the surface of the vdWH. In vacuum, a significant fraction of the molecular adsorbates are removed, including through laser-assisted desorption. These adsorbates are efficient electron traps [49,51,81], acting against the net photoinduced electron transfer from $MoSe_2$ to graphene. In the absence of molecular adsorbates, the electrons that are transferred from $MoSe_2$ to graphene reside in graphene as long as the laser illumination is on (see Sec. VI). Such extrinsic effects impact the optoelectronic response of 2DM and vdWH—most often examined under ambient conditions—and therefore provide an impetus for further studies under controlled atmospheres [49], using different substrates, stacking sequences, and encapsulating materials [62–64]. Along this line, we have studied [see Fig. 5(b) and Ref. [52], Fig. S11) a $MoSe_2/Gr/SiO_2$ vdWH. Remarkably, the results obtained on this *inverted* heterostructure are very similar to those obtained on $Gr/MoSe_2/SiO_2$ vdWHs.

Finally, we have compared the PL in $Gr/MoSe_2/SiO_2$ and $MoSe_2/Gr/SiO_2$ in ambient air and under vacuum conditions. While the PL of bare $MoSe_2$ is—as previously reported [81]—quenched under vacuum, the PL intensity and line shape measured as a function of Φ_{ph} in ambient air and under vacuum in $Gr/MoSe_2$ are not appreciably different (see Fig. 6 and Ref. [52], Fig. S12).

VI. DISCUSSION

The complementary results reported in Secs. III–V now make it possible to address a set of open questions of high relevance for fundamental photophysics and optoelectronic applications. What are the microscopic mechanisms responsible for net electron transfer and its saturation (Sec. VI A)? What is the impact of excitonic effects on interlayer coupling (Sec. VI B)? What are the relative contributions of ICT and IET to the massive photoluminescence quenching analyzed in Fig. 2 (Sec. VI C)?

A. Charge transfer mechanism

The clear saturation of the net photoinduced ICT in Gr/TMD heterostructures shown in Fig. 5 has not been reported thus far, and we first discuss the underlying microscopic ICT mechanisms. Since the Dirac point of graphene is located between the valence band maximum and the conduction band minimum of $MoSe_2$ [83–85], the tunneling of photoexcited electrons *and* holes to graphene can be envisioned as long as energy and momentum are conserved and E_F^{Gr} lies sufficiently below (above) the conduction band minimum (valence band maximum) of $MoSe_2$. Electron transfer and hole transfer to graphene are sketched in Figs. 7(a) and 7(b). To account for our experimental findings, we propose the following scenario.

The band structure of coupled $Gr/MoSe_2$ can be, in a first approximation, considered as the superposition of the bands of the different materials [23,86] separated by a subnanometer "van der Waals gap." The relative position of the band structure is determined by the offsets between the Dirac point of graphene and the valence (conduction) band maximum (minimum) of $MoSe_2$. In the dark, without loss of generality, we may assume that both graphene and $MoSe_2$ are quasineutral. When visible light is shined onto $Gr/MoSe_2$, electron-hole pairs and excitons are mainly created in $MoSe_2$ since the latter absorbs significantly more

than graphene [27,54]. At this point, given the very close electron and hole effective masses in $MoSe_2$ [87], the rates of photoinduced electron and hole transfer from $MoSe_2$ to graphene will chiefly depend on the wave-function overlap, the density of states in graphene, and the energy difference between the band extrema in $MoSe_2$ and E_F^{Gr}.

Assuming the Dirac point lies closer to the valence band maximum than to the conduction band minimum [83,84], the photoinduced electron current to graphene should exceed the hole current immediately after sample illumination, consistently with our experimental findings. Because of the small density of states of graphene near its Dirac point [12], the net electron transfer to graphene induces a sizable rise of E_F^{Gr} above the Dirac point. Thus, as E_F^{Gr} moves away from the valence band maximum in $MoSe_2$, the hole current to *n*-doped graphene increases significantly. The vanishing of the net electron transfer to graphene then results from the cancellation of the photoinduced electron [Fig. 7(a)] and hole [Fig. 7(b)] currents. In vacuum and in the absence of adsorbates, this saturation is reached in the steady state at any Φ_{ph}. In ambient air, electrons may escape from graphene (in $Gr/MoSe_2/SiO_2$) or $MoSe_2$ (in $MoSe_2/Gr/SiO_2$), resulting (at intermediate $\Phi_{ph} < 10^{23}$ cm^{-2} s^{-1}) in a steady-state E_F^{Gr} below the Φ_{ph}-independent saturation value observed in vacuum [see Fig. 5(b)] [88].

The very similar saturation values of E_F^{Gr} uncovered in several $Gr/MoSe_2$ samples both in ambient air *and* in vacuum (see Fig. 5) suggest a limit set by the intrinsic band offsets between graphene and $MoSe_2$, as well as the electron and hole tunneling efficiencies. The latter are affected by extrinsic materials properties, such as the presence of band-tail states as well as other traps and defects [89]. Systematic studies using other TMDs with distinct band offsets relative to graphene and controlled amounts of impurities and/or defects will help determine the extrinsic and intrinsic effects in the net charge transfer saturation. Nevertheless, our work is a step towards the optical determination of band offsets in van der Waals heterostructures. Confronted with electron transport measurements [90], or angle-resolved photoemission spectroscopy [23,85], our Raman-based approach may unveil the impact of strong band-gap renormalization and exciton binding energy on the optoelectronic properties of TMDs and related vdWHs.

B. Impact of excitonic effects

Indeed, although PL measurements (see Fig. 2) make it clear that excitons are formed in $MoSe_2$, the impact of excitonic effects on interlayer coupling and, more generally, on the optoelectronic response of vdWH remains elusive.

Upon optical excitation well beyond the optical band gap (as is the case in Figs. 1–6), free electron-hole pairs *and* tightly bound excitons can be formed in $Gr/MoSe_2$ [60,62]. Despite exciton formation being highly efficient and occurring on subpicosecond to a few picosecond time scales [68,91], our PL measurements have revealed equally short band-edge (*A*) exciton lifetimes in $Gr/MoSe_2$ (see Fig 2). Therefore, the observed interlayer coupling processes may certainly involve band-edge excitons but may also imply direct *hot* carrier and/or higher-order exciton transfer to graphene. To assess the contribution of out-of-equilibrium effects, we have combined PL and Raman measurements in ambient air and in vacuum on a $Gr/WS_2/SiO_2$ vdWH at two different laser photon energies near the *B* exciton (2.33 eV) and slightly below the *A* exciton (1.96 eV). In the latter case, only *A* excitons can be formed by means of an upconversion process [92,93] (see Ref. [52], Fig. S14). For both incoming photon energies, we observe strong PL quenching, as well as photoinduced doping, very similar to the observations discussed in Figs. 2–6 for $Gr/MoSe_2$ vdWHs. These observations indicate that ICT and IET processes in GR/TMD vdWH mainly involve band-edge TMD excitons [94]. This result illustrates the unusually strong excitonic effects in TMDs, which must be taken into consideration when adapting free-carrier optoelectronic models to the case of vdWH-based devices.

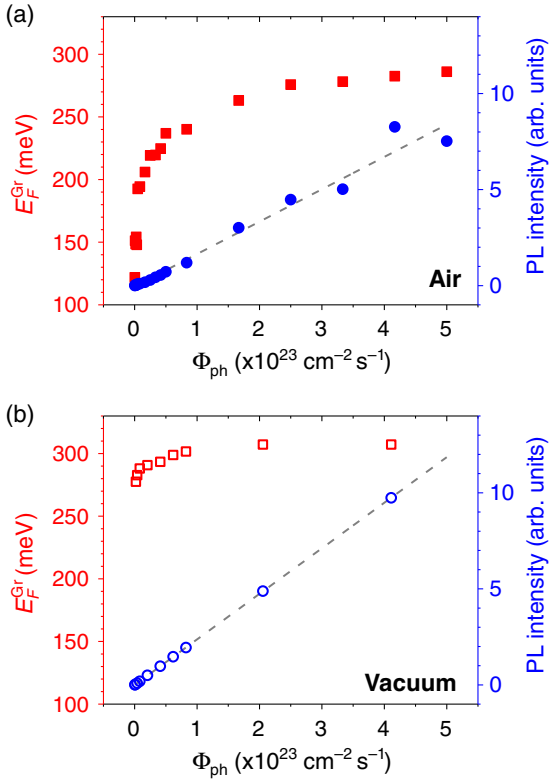

FIG. 6. Comparison between the dependence of the Fermi energy in graphene E_F^{Gr} (left axis, red) and the PL intensity of the A exciton in $MoSe_2$ I_{PL}^A (right axis, blue) on Φ_{ph}, measured on sample S_2 (a) in ambient air and (b) in vacuum at a laser photon energy of 2.33 eV. The dashed lines are linear fits to the photoluminescence data.

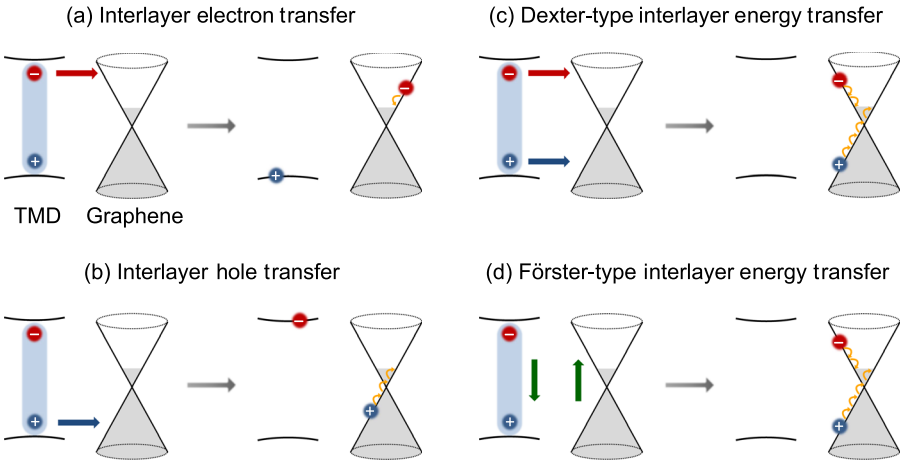

FIG. 7. Sketches, in momentum-energy space, of interlayer (a) electron and (b) hole transfer, and (c) Dexter-type and (d) Förster-type energy-transfer processes from monolayer TMD to graphene. Band-edge (A) excitons are shown by the blue shaded area, with the electron in red and the hole in dark blue. The curved dark yellow arrows represent ultrafast energy relaxation of transferred carriers in graphene down to the Fermi level. In the case of balanced electron and hole flows to graphene, the charge transfer processes effectively result in energy transfer.

C. Charge vs energy transfer

Finally, we address the competition between ICT and IET. Let us first recall that Raman measurements probe the steady-state charge carrier densities in our samples and do not make it possible to extract electron and hole transfer rates. Figure 6 summarizes our findings by confronting the dependence of E_F^{Gr} and I_{PL}^{A} on Φ_{ph} in sample S_2. The key implications of our combined PL and Raman study are that the short exciton lifetime in $\mathrm{Gr}/\mathrm{MoSe_2}$ is (i) independent of Φ_{ph} (over nearly 4 orders of magnitude), (ii) unaffected by the environmental conditions (air vs vacuum), and, crucially, (iii) unaffected by the presence (in air, at low Φ_{ph}) or absence (in vacuum at any Φ_{ph}, or in air at high Φ_{ph}) of *net* photoinduced ICT (here, electron transfer from $\mathrm{MoSe_2}$ to graphene; see also Ref. [52], Fig. S13).

Our data demonstrate that, although electrons and holes may transfer to graphene, ICT processes alone (even in the case of balanced electron and hole transfer) cannot be responsible for the massive PL quenching and linear rise of the PL intensity vs Φ_{ph}. Instead, IET—either in the form of electron exchange [i.e., Dexter-type IET, Fig. 7(c)] or dipole-dipole interaction [i.e., Förster-type IET, Fig. 7(d)]—provides a highly efficient relaxation pathway for excitons in Gr/TMD heterostructures.

Consequently, the exciton lifetime of about 1 ps deduced from PL measurements (see Sec. III) can be considered as a fair estimation of the energy-transfer time scale from a TMD monolayer to a graphene monolayer placed in its immediate vicinity. Since interlayer coupling is highly sensitive to minute changes (at the Å level) in the distance between 2D layers as well as to the distribution of TMD excitons in energy-momentum space [42,68], a timely theoretical and experimental challenge is to unravel the distance and temperature dependence of the energy-transfer rate and quantify contributions stemming from short-range (Dexter) and longer-range (Förster) mechanisms.

Let us add the following comments in order to tentatively pinpoint the microscopic energy-transfer mechanism. First, although balanced ICT and Dexter-type IET follow *a priori* two distinct microscopic mechanisms [see Figs. 7(a)–7(c)], both processes imply charge tunneling (i.e., wave-function overlap) and result in a similar final state where the energy of an exciton population is transferred to graphene. Interestingly, it was recently predicted in porphyrin/graphene hybrids that Dexter ET is largely inefficient compared to Förster ET even at subnanometer distances [95]. In the case of Gr/TMD vdWHs, the large in-plane dipoles in monolayer TMDs [96] should further favor Förster energy transfer to graphene. Along this line, the exciton lifetime measured in *decoupled* $\mathrm{Gr}/\mathrm{MoSe_2}/\mathrm{SiO_2}$ [see Fig. 2(e)] is of the same order of magnitude yet appreciably shorter than in $\mathrm{MoSe_2}/\mathrm{SiO_2}$, an effect that may tentatively be assigned to long-range Förster energy transfer [97].

VII. CONCLUSION AND OUTLOOK

We have exploited complementary insights from micro-Raman and photoluminescence spectroscopies to disentangle contributions from interlayer charge and energy transfer in graphene/TMD heterostructures and establish the key role of energy transfer. These general findings advance our fundamental understanding of light-matter interactions at atomically thin heterointerfaces and have far-reaching consequences for applications.

Indeed, the graphene/TMD system is a ubiquitous building block in emerging optoelectronic nanodevices. Having established that band-edge TMD excitons transfer to graphene with near-unity efficiency, a key challenge is

now to separate the electron-hole pairs formed in graphene [98] and enhance photoconductivity and/or photocurrent generation before these charge carriers release their energy into heat on a subpicosecond time scale [99,100].

The competition between interlayer charge and energy transfer is also a matter of active debate in related systems, e.g., in TMD/TMD type-II heterojunctions [32–37], which are also of high relevance for optoelectronics [10] and valleytronics [31]. We have shown that fingerprints of interlayer charge transfer are encoded in the Raman response of TMD monolayers. Combining Raman measurements and photoluminescence spectroscopy of intralayer and interlayer excitons should provide a more comprehensive picture of exciton dynamics in these atomically thin semiconductor heterostructures.

More broadly, van der Waals heterostructures are also an emerging platform to explore many-body effects and new regimes of strong and/or chiral light-matter interactions. Further developments in these areas will benefit from the present insights into interlayer charge and energy transfer.

ACKNOWLEDGMENTS

We thank D. M. Basko, C. Robert, D. Lagarde, X. Marie, A. Ouerghi, G. Schull, and C. Genet for fruitful discussions. We are grateful to J. Chrétien for his early contribution to experimental measurements, to H. Majjad and M. Rastei for help with AFM measurements, and to the StNano clean room staff and M. Romeo for technical assistance. We acknowledge financial support from the Agence Nationale de la Recherche (under Grant No. H2DH ANR-15-CE24-0016) and from the LabEx NIE (under Grant No. ANR-11-LABX-0058-NIE within the Investissement d'Avenir program ANR-10-IDEX-0002-02). S. B. is a member of Institut Universitaire de France (IUF).

APPENDIX: EXPERIMENTAL DETAILS

$Gr/MoSe_2$ vdWHs were prepared on Si wafers covered with a 90-nm-thick SiO_2 epilayer using a viscoelastic transfer technique [101]. The $Gr/MoSe_2$ vdWHs were first characterized by AFM and then by micro-PL and micro-Raman measurements. As-prepared samples [such as sample S_1 discussed above; see Fig. 1(a)] as well as annealed samples (1 hour at 150 °C and 2 hours at 200 °C in high vacuum) such as sample S_3 were studied. Although more contamination "pockets" (see Ref. [52], Fig. S1) are present on as-prepared samples, we could observe, both in annealed and as-prepared samples, extended ($>25\ \mu m^2$) *coupled* $Gr/MoSe_2$ domains with smooth and uniform interfaces due to a self-cleaning process [11].

PL and Raman studies were carried out in ambient air and in high vacuum, in a backscattering geometry, using a home-built confocal microscope. Unless otherwise noted, the samples were optically excited using a single longitudinal-mode, linearly polarized, 2.33-eV (532-nm) continuous-wave laser. The collected light was dispersed onto a charged-coupled-device array by a single (500 nm in focal length) monochromator equipped with a 150 (resp. 900 for graphene, 2400 for $MoSe_2$) grooves/mm grating for PL (resp. Raman) measurements. Spectral resolutions of 1.4 cm^{-1} and 0.6 cm^{-1} were obtained for Raman measurements with the 900 and 2400 grooves/mm grating, respectively. The sample holder was mounted onto a *x-y-z* piezoelectric stage, allowing hyperspectral imaging. Time-resolved PL measurements were performed on the same setup using a pulsed supercontinuum laser, with a repetition rate tunable from 1.95 MHz up to 78 MHz. The unpolarized output of the supercontinuum laser at 1.96 eV (633 nm) was selected using an acousto-optic tunable filter. PL decays were obtained using an avalanche photodiode coupled to a time-tagged, time-correlated, single-photon counting board. We have employed a very broad range of incident photon fluxes, resulting in exciton densities below and beyond the values achieved in earlier works [18,20,59]. The incident photon flux Φ_{ph} was obtained by measuring the laser power and the area of the laser spot. For instance, with a measured optical power of 1 μW at the objective at 2.33 eV, we obtained a photon flux of $2.2 \times 10^{21}\ cm^{-2}\ s^{-1}$ using a 100x objective with a numerical aperture of 0.9. The Raman peaks were fit using Lorentzian and modified Lorentzian [48,56] profiles for the *G*- and 2*D*-mode features, respectively, and Voigt profiles (with a fixed Gaussian width taking into account our spectral resolution) for $MoSe_2$ features. Therefore, in Fig. 4(b), the linewidth $\Gamma_{A_1'}$ has to be understood as the Lorentzian FWHM extracted from a Voigt fit.

[1] T. Förster, *Intermolecular energy migration and fluorescence*, Ann. Phys. (Berlin) **437**, 55 (1948).
[2] R. van Grondelle, J. P. Dekker, T. Gillbro, and V. Sundstrom, *Energy Transfer and Trapping in Photosynthesis*, Biochim. Biophys. Acta **1187**, 1 (1994).
[3] B. Guzelturk and H. V. Demir, *Near-Field Energy Transfer Using Nanoemitters for Optoelectronics*, Adv. Funct. Mater. **26**, 8158 (2016).
[4] A. Govorov, P. L. Hernández Martínez, and H. V. Demir, *Understanding and Modeling Förster-type Resonance Energy Transfer (FRET)* (Springer, New York, 2016).
[5] V. May and O. Kühn, *Charge and Energy Transfer Dynamics in Molecular Systems* (John Wiley & Sons, New York, 2008).
[6] S. M. Sze and K. K. Ng, *Physics of Semiconductor Devices* (John Wiley & Sons, New York, 2006).
[7] D. L. Dexter, *A Theory of Sensitized Luminescence in Solids*, J. Chem. Phys. **21**, 836 (1953).
[8] A. K. Geim and I. V. Grigorieva, *Van der Waals Heterostructures*, Nature (London) **499**, 419 (2013).
[9] K. S. Novoselov, A. Mishchenko, A. Carvalho, and A. H. Castro Neto, *2D Materials and van der Waals Heterostructures*, Science **353**, aac9439 (2016).

[10] K. F. Mak and J. Shan, *Photonics and Optoelectronics of 2D Semiconductor Transition Metal Dichalcogenides*, Nat. Photonics **10**, 216 (2016).
[11] S. J. Haigh, A. Gholinia, R. Jalil, S. Romani, L. Britnell, D. C. Elias, K. S. Novoselov, L. A. Ponomarenko, A. K. Geim, and R. Gorbachev, *Cross-Sectional Imaging of Individual Layers and Buried Interfaces of Graphene-Based Heterostructures and Superlattices*, Nat. Mater. **11**, 764 (2012).
[12] A. H. Castro Neto, F. Guinea, N. M. R. Peres, K. S. Novoselov, and A. K. Geim, *The Electronic Properties of Graphene*, Rev. Mod. Phys. **81**, 109 (2009).
[13] K. F. Mak, C. Lee, J. Hone, J. Shan, and T. F. Heinz, *Atomically Thin* MoS_2*: A New Direct-Gap Semiconductor*, Phys. Rev. Lett. **105**, 136805 (2010).
[14] A. Splendiani, L. Sun, Y. Zhang, T. Li, J. Kim, C.-Y. Chim, G. Galli, and F. Wang, *Emerging Photoluminescence in Monolayer* MoS_2, Nano Lett. **10**, 1271 (2010).
[15] L. Britnell, R. M. Ribeiro, A. Eckmann, R. Jalil, B. D. Belle, A. Mishchenko, Y.-J. Kim, R. V. Gorbachev, T. Georgiou, S. V. Morozov *et al.*, *Strong Light-Matter Interactions in Heterostructures of Atomically Thin Films*, Science **340**, 1311 (2013).
[16] W. J. Yu, Y. Liu, H. Zhou, A. Yin, Z. Li, Y. Huang, and X. Duan, *Highly Efficient Gate-Tunable Photocurrent Generation in Vertical Heterostructures of Layered Materials*, Nat. Nanotechnol. **8**, 952 (2013).
[17] K. Roy, M. Padmanabhan, S. Goswami, T. Phanindra Sai, G. Ramalingam, S. Raghavan, and A. Ghosh, *Graphene-*MoS_2 *Hybrid Structures for Multifunctional Photoresponsive Memory Devices*, Nat. Nanotechnol. **8**, 826 (2013).
[18] W. Zhang, C.-P. Chuu, J.-K. Huang, C.-H. Chen, M.-L. Tsai, Y.-H. Chang, C.-T. Liang, Y.-Z. Chen, Y.-L. Chueh, J.-H. He, M.-Y. Chou, and L.-J. Li, *Ultrahigh-Gain Photodetectors Based on Atomically Thin Graphene-*MoS_2 *Heterostructures*, Sci. Rep. **4**, 3826 (2014).
[19] D. De Fazio, I. Goykhman, D. Yoon, M. Bruna, A. Eiden, S. Milana, U. Sassi, M. Barbone, D. Dumcenco, K. Marinov, A. Kis, and A. C. Ferrari, *High Responsivity, Large-Area* Graphene/MoS_2 *Flexible Photodetectors*, ACS Nano **10**, 8252 (2016).
[20] M. Massicotte, P. Schmidt, F. Vialla, K. G. Schädler, A. Reserbat-Plantey, K. Watanabe, T. Taniguchi, K. J. Tielrooij, and F. H. L. Koppens, *Picosecond Photoresponse in van der Waals Heterostructures*, Nat. Nanotechnol. **11**, 42 (2016).
[21] K. M. McCreary, A. T. Hanbicki, J. T. Robinson, E. Cobas, J. C. Culbertson, A. L. Friedman, G. G. Jernigan, and B. T. Jonker, *Large-Area Synthesis of Continuous and Uniform* MoS_2 *Monolayer Films on Graphene*, Adv. Funct. Mater. **24**, 6449 (2014).
[22] G. W. Shim, K. Yoo, S.-B. Seo, J. Shin, D. Y. Jung, I.-S. Kang, C. W. Ahn, B. J. Cho, and S.-Y. Choi, *Large-Area Single-Layer* $MoSe_2$ *and Its van der Waals Heterostructures*, ACS Nano **8**, 6655 (2014).
[23] D. Pierucci, H. Henck, J. Avila, A. Balan, C. H. Naylor, G. Patriarche, Y. J. Dappe, M. G. Silly, F. Sirotti, A. T. Charlie Johnson *et al.*, *Band Alignment and Minigaps in Monolayer* MoS_2*-Graphene van der Waals Heterostructures*, Nano Lett. **16**, 4054 (2016).
[24] J. He, N. Kumar, M. Z. Bellus, H.-Y. Chiu, D. He, Y. Wang, and H. Zhao, *Electron Transfer and Coupling in Graphene–Tungsten Disulfide van der Waals Heterostructures*, Nat. Commun. **5**, 5622 (2014).
[25] H. Henck, D. Pierucci, J. Chaste, C. H. Naylor, J. Avila, A. Balan, M. G. Silly, M. C. Asensio, F. Sirotti, A. T. C. Johnson, E. Lhuillier, and A. Ouerghi, *Electrolytic Phototransistor Based on Graphene-*MoS_2 *van der Waals p-n Heterojunction with Tunable Photoresponse*, Appl. Phys. Lett. **109**, 113103 (2016).
[26] F. H. L. Koppens, T. Mueller, Ph. Avouris, A. C. Ferrari, M. S. Vitiello, and M. Polini, *Photodetectors Based on Graphene, Other Two-Dimensional Materials and Hybrid Systems*, Nat. Nanotechnol. **9**, 780 (2014).
[27] K. F. Mak, L. Ju, F. Wang, and T. F. Heinz, *Optical Spectroscopy of Graphene: From the Far Infrared to the Ultraviolet*, Solid State Commun. **152**, 1341 (2012).
[28] K.-J. Tielrooij, L. Piatkowski, M. Massicotte, A. Woessner, Q. Ma, Y. Lee, K. S. Myhro, C. N. Lau, P. Jarillo-Herrero, N. F. van Hulst *et al.*, *Generation of Photovoltage in Graphene on a Femtosecond Timescale through Efficient Carrier Heating*, Nat. Nanotechnol. **10**, 437 (2015).
[29] G. Wang, A. Chernikov, M. M. Glazov, T. F. Heinz, X. Marie, T. Amand, and B. Urbaszek, *Excitons in Atomically Thin Transition Metal Dichalcogenides*, arXiv:1707.05863.
[30] F. Xia, H. Wang, D. Xiao, M. Dubey, and A. Ramasubramaniam, *Two-Dimensional Material Nanophotonics*, Nat. Photonics **8**, 899 (2014).
[31] J. R. Schaibley, H. Yu, G. Clark, P. Rivera, J. S. Ross, K. L. Seyler, W. Yao, and X. Xu, *Valleytronics in 2D Materials*, Nat. Rev. Mater. **1**, 16055 (2016).
[32] F. Ceballos, M. Z. Bellus, H.-Y. Chiu, and H. Zhao, *Ultrafast Charge Separation and Indirect Exciton Formation in a* $MoS_2 - MoSe_2$ *van der Waals Heterostructure*, ACS Nano **8**, 12717 (2014).
[33] X. Hong, J. Kim, S.-F. Shi, Y. Zhang, C. Jin, Y. Sun, S. Tongay, J. Wu, Y. Zhang, and F. Wang, *Ultrafast Charge Transfer in Atomically Thin* MoS_2/WS_2 *Heterostructures*, Nat. Nanotechnol. **9**, 682 (2014).
[34] H. Fang, C. Battaglia, C. Carraro, S. Nemsak, B. Ozdol, J. S. Kang, H. A. Bechtel, S. B. Desai, F. Kronast, A. A. Unal, G. Conti, C. Conlon, G. K. Palsson, M. C. Martin, A. M. Minor, C. S. Fadley, E. Yablonovitch, R. Maboudian, and A. Javey, *Strong Interlayer Coupling in van der Waals Heterostructures Built from Single-Layer Chalcogenides*, Proc. Natl. Acad. Sci. U.S.A. **111**, 6198 (2014).
[35] C.-H. Lee, G.-H. Lee, A. M. van der Zande, W. Chen, Y. Li, M. Han, X. Cui, G. Arefe, C. Nuckolls, T. F. Heinz, J. Guo, J. Hone, and P. Kim, *Atomically Thin p-n Junctions with van der Waals Heterointerfaces*, Nat. Nanotechnol. **9**, 676 (2014).
[36] P. Rivera, J. R. Schaibley, A. M. Jones, J. S. Ross, S. Wu, G. Aivazian, P. Klement, K. Seyler, G. Clark, N. J. Ghimire *et al.*, *Observation of Long-Lived Interlayer Excitons in Monolayer* $MoSe_2-WSe_2$ *Heterostructures*, Nat. Commun. **6**, 6242 (2015).
[37] D. Kozawa, A. Carvalho, I. Verzhbitskiy, F. Giustiniano, Y. Miyauchi, S. Mouri, A. H. Castro Neto, K. Matsuda, and G. Eda, *Evidence for Fast Interlayer Energy Transfer in*

$MoSe_2/WS_2$ *Heterostructures*, Nano Lett. **16**, 4087 (2016).

[38] C. Roquelet, D. Garrot, J.-S. Lauret, C. Voisin, V. Alain-Rizzo, Ph. Roussignol, J. A. Delaire, and E. Deleporte, *Quantum Efficiency of Energy Transfer in Noncovalent Carbon Nanotube/Porphyrin Compounds*, Appl. Phys. Lett. **97**, 141918 (2010).

[39] Z. Chen, S. Berciaud, C. Nuckolls, T. F. Heinz, and L. E. Brus, *Energy Transfer from Individual Semiconductor Nanocrystals to Graphene*, ACS Nano **4**, 2964 (2010).

[40] L. Gaudreau, K. J. Tielrooij, G. E. D. K. Prawiroatmodjo, J. Osmond, F. J. García de Abajo, and F. H. L. Koppens, *Universal Distance-Scaling of Nonradiative Energy Transfer to Graphene*, Nano Lett. **13**, 2030 (2013).

[41] J. Tisler, T. Oeckinghaus, R. J. Sthr, R. Kolesov, R. Reuter, F. Reinhard, and J. Wrachtrup, *Single Defect Center Scanning Near-Field Optical Microscopy on Graphene*, Nano Lett. **13**, 3152 (2013).

[42] F. Federspiel, G. Froehlicher, M. Nasilowski, S. Pedetti, A. Mahmood, B. Doudin, S. Park, J.-O. Lee, D. Halley, B. Dubertret *et al.*, *Distance Dependence of the Energy Transfer Rate from a Single Semiconductor Nanostructure to Graphene*, Nano Lett. **15**, 1252 (2015).

[43] F. Prins, A. J. Goodman, and W. A. Tisdale, *Reduced Dielectric Screening and Enhanced Energy Transfer in Single- and Few-Layer* MoS_2, Nano Lett. **14**, 6087 (2014).

[44] A. Raja, A. Montoya-Castillo, J. Zultak, X.-X. Zhang, Z. Ye, C. Roquelet, D. A. Chenet, A. M. van der Zande, P. Huang, S. Jockusch *et al.*, *Energy Transfer from Quantum Dots to Graphene and* MoS_2*: The Role of Absorption and Screening in Two-Dimensional Materials*, Nano Lett. **16**, 2328 (2016).

[45] J. Yan, Y. Zhang, P. Kim, and A. Pinczuk, *Electric Field Effect Tuning of Electron-Phonon Coupling in Graphene*, Phys. Rev. Lett. **98**, 166802 (2007).

[46] S. Pisana, M. Lazzeri, C. Casiraghi, K. S. Novoselov, A. K. Geim, A. C. Ferrari, and F. Mauri, *Breakdown of the Adiabatic Born-Oppenheimer Approximation in Graphene*, Nat. Mater. **6**, 198 (2007).

[47] A. Das, S. Pisana, B. Chakraborty, S. Piscanec, S. K. Saha, U. V. Waghmare, K. S. Novoselov, H. R. Krishnamurthy, A. K. Geim, A. C. Ferrari, and A. K. Sood, *Monitoring Dopants by Raman Scattering in an Electrochemically Top-Gated Graphene Transistor*, Nat. Nanotechnol. **3**, 210 (2008).

[48] G. Froehlicher and S. Berciaud, *Raman Spectroscopy of Electrochemically Gated Graphene Transistors: Geometrical Capacitance, Electron-Phonon, Electron-Electron, and Electron-Defect Scattering*, Phys. Rev. B **91**, 205413 (2015).

[49] S. Ryu, L. Liu, S. Berciaud, Y.-J. Yu, H. Liu, P. Kim, G. W. Flynn, and L. E. Brus, *Atmospheric Oxygen Binding and Hole Doping in Deformed Graphene on a* SiO_2 *Substrate*, Nano Lett. **10**, 4944 (2010).

[50] B. Chakraborty, A. Bera, D. V. S. Muthu, S. Bhowmick, U. V. Waghmare, and A. K. Sood, *Symmetry-Dependent Phonon Renormalization in Monolayer* MoS_2 *Transistor*, Phys. Rev. B **85**, 161403 (2012).

[51] B. Miller, E. Parzinger, A. Vernickel, A. W. Holleitner, and U. Wurstbauer, *Photogating of Mono- and Few-Layer* MoS_2, Appl. Phys. Lett. **106**, 122103 (2015).

[52] See Supplemental Material at http://link.aps.org/supplemental/10.1103/PhysRevX.8.011007 for details on atomic force microscopy, Raman spectra of graphene and $MoSe_2$ for increasing Φ_{ph}, details on spatially resolved Raman studies, additional photoluminescence and Raman measurements, discussion on the frequency of the Raman 2D-mode feature in $Gr/MoSe_2$, and discussion on optical interference effects.

[53] A. C. Ferrari and D. M. Basko, *Raman Spectroscopy as a Versatile Tool for Studying the Properties of Graphene*, Nat. Nanotechnol. **8**, 235 (2013).

[54] Y. Li, A. Chernikov, X. Zhang, A. Rigosi, H. M. Hill, A. M. van der Zande, D. A. Chenet, E.-M. Shih, J. Hone, and T. F. Heinz, *Measurement of the Optical Dielectric Function of Monolayer Transition-Metal Dichalcogenides:* MoS_2, $MoSe_2$, WS_2, *and* WSe_2, Phys. Rev. B **90**, 205422 (2014).

[55] J. E. Lee, G. Ahn, J. Shim, Y. S. Lee, and S. Ryu, *Optical Separation of Mechanical Strain from Charge Doping in Graphene*, Nat. Commun. **3**, 1024 (2012).

[56] D. Metten, F. Federspiel, M. Romeo, and S. Berciaud, *All-Optical Blister Test of Suspended Graphene Using Micro-Raman Spectroscopy*, Phys. Rev. Applied **2**, 054008 (2014).

[57] G. Ahn, H. R. Kim, T. Y. Ko, K. Choi, K. Watanabe, T. Taniguchi, B. H. Hong, and S. Ryu, *Optical Probing of the Electronic Interaction Between Graphene and Hexagonal Boron Nitride*, ACS Nano **7**, 1533 (2013).

[58] F. Forster, A. Molina-Sanchez, S. Engels, A. Epping, K. Watanabe, T. Taniguchi, L. Wirtz, and C. Stampfer, *Dielectric Screening of the Kohn Anomaly of Graphene on Hexagonal Boron Nitride*, Phys. Rev. B **88**, 085419 (2013).

[59] K. He, N. Kumar, L. Zhao, Z. Wang, K. F. Mak, H. Zhao, and J. Shan, *Tightly Bound Excitons in Monolayer* WSe_2, Phys. Rev. Lett. **113**, 026803 (2014).

[60] M. M. Ugeda, A. J. Bradley, S.-F. Shi, F. H. da Jornada, Y. Zhang, D. Y. Qiu, W. Ruan, S.-K. Mo, Z. Hussain, Z.-X. Shen, F. Wang, S. G. Louie, and M. F. Crommie, *Giant Bandgap Renormalization and Excitonic Effects in a Monolayer Transition Metal Dichalcogenide Semiconductor*, Nat. Mater. **13**, 1091 (2014).

[61] A. V. Stier, N. P. Wilson, G. Clark, X. Xu, and S. A. Crooker, *Probing the Influence of Dielectric Environment on Excitons in Monolayer* WSe_2*: Insight from High Magnetic Fields*, Nano Lett. **16**, 7054 (2016).

[62] A. Raja, A. Chaves, J. Yu, G. Arefe, H. M. Hill, A. F. Rigosi, T. C. Berkelbach, P. Nagler, C. Schüller, T. Korn *et al.*, *Coulomb Engineering of the Bandgap and Excitons in Two-Dimensional Materials*, Nat. Commun. **8**, 15251 (2017).

[63] F. Cadiz, E. Courtade, C. Robert, G. Wang, Y. Shen, H. Cai, T. Taniguchi, K. Watanabe, H. Carrere, D. Lagarde, M. Manca, T. Amand, P. Renucci, S. Tongay, X. Marie, and B. Urbaszek, *Excitonic Linewidth Approaching the Homogeneous Limit in* MoS_2*-Based van der Waals Heterostructures*, Phys. Rev. X **7**, 021026 (2017).

[64] O. A. Ajayi, J. V. Ardelean, G. D. Shepard, J. Wang, A. Antony, T. Taniguchi, K. Watanabe, T. F. Heinz, S. Strauf, X.-Y. Zhu, and J. C. Hone, *Approaching the Intrinsic*

Photoluminescence Linewidth in Transition Metal Dichalcogenide Monolayers, 2D Mater. **4**, 031011 (2017).

[65] N. Kumar, Q. Cui, F. Ceballos, D. He, Y. Wang, and H. Zhao, *Exciton-Exciton Annihilation in* $MoSe_2$ *Monolayers*, Phys. Rev. B **89**, 125427 (2014).

[66] S. Mouri, Y. Miyauchi, M. Toh, W. Zhao, G. Eda, and K. Matsuda, *Nonlinear Photoluminescence in Atomically Thin Layered* WSe_2 *Arising from Diffusion-Assisted Exciton-Exciton Annihilation*, Phys. Rev. B **90**, 155449 (2014).

[67] H. Shi, R. Yan, S. Bertolazzi, J. Brivio, B. Gao, A. Kis, D. Jena, H. G. Xing, and L. Huang, *Exciton Dynamics in Suspended Monolayer and Few-Layer* MoS_2 *2D Crystals*, ACS Nano **7**, 1072 (2013).

[68] C. Robert, D. Lagarde, F. Cadiz, G. Wang, B. Lassagne, T. Amand, A. Balocchi, P. Renucci, S. Tongay, B. Urbaszek, and X. Marie, *Exciton Radiative Lifetime in Transition Metal Dichalcogenide Monolayers*, Phys. Rev. B **93**, 205423 (2016).

[69] S. Berciaud, S. Ryu, L. E. Brus, and T. F. Heinz, *Probing the Intrinsic Properties of Exfoliated Graphene: Raman Spectroscopy of Free-Standing Monolayers*, Nano Lett. **9**, 346 (2009).

[70] A. A. Balandin, *Thermal Properties of Graphene and Nanostructured Carbon Materials*, Nat. Mater. **10**, 569 (2011).

[71] T. Ando, *Anomaly of Optical Phonon in Monolayer Graphene*, J. Phys. Soc. Jpn. **75**, 124701 (2006).

[72] J. S. Ross, S. Wu, H. Yu, N. J. Ghimire, A. M. Jones, G. Aivazian, J. Yan, D. G. Mandrus, D. Xiao, W. Yao *et al.*, *Electrical Control of Neutral and Charged Excitons in a Monolayer Semiconductor*, Nat. Commun. **4**, 1474 (2013).

[73] P. Soubelet, A. E. Bruchhausen, A. Fainstein, K. Nogajewski, and C. Faugeras, *Resonance Effects in the Raman Scattering of Monolayer and Few-Layer* $MoSe_2$, Phys. Rev. B **93**, 155407 (2016).

[74] X. Zhang, X.-F. Qiao, W. Shi, J.-B. Wu, D.-S. Jiang, and P.-H. Tan, *Phonon and Raman Scattering of Two-Dimensional Transition Metal Dichalcogenides from Monolayer, Multilayer to Bulk Material*, Chem. Soc. Rev. **44**, 2757 (2015).

[75] K.-G. Zhou, F. Withers, Y. Cao, S. Hu, G. Yu, and C. Casiraghi, *Raman Modes of* MoS_2 *Used as Fingerprint of van der Waals Interactions in 2-D Crystal-Based Heterostructures*, ACS Nano **8**, 9914 (2014).

[76] X. Luo, Y. Zhao, J. Zhang, Q. Xiong, and S. Y. Quek, *Anomalous Frequency Trends in* MoS_2 *Thin Films Attributed to Surface Effects*, Phys. Rev. B **88**, 075320 (2013).

[77] G. Froehlicher, E. Lorchat, F. Fernique, C. Joshi, A. Molina-Sánchez, L. Wirtz, and S. Berciaud, *Unified Description of the Optical Phonon Modes in N-Layer* $MoTe_2$, Nano Lett. **15**, 6481 (2015).

[78] The observed upshift may, in part, stem from van der Waals coupling between the graphene and $MoSe_2$ monolayers [74–77] (similarly to the case of TMD bilayers), as well as from surface effects [76,77], i.e., in the present case, slightly larger force constants between Mo and Se atoms in $Gr/MoSe_2/SiO_2$ than in $air/MoSe_2/SiO_2$. However, neither kind of effect would lead to the significant narrowing of the A_1' feature observed in $Gr/MoSe_2/SiO_2$, and they cannot account for the differential effects shown in Fig. 4(c).

[79] H. J. Conley, B. Wang, J. I. Ziegler, R. F. Haglund, S. T. Pantelides, and K. I. Bolotin, *Bandgap Engineering of Strained Monolayer and Bilayer* MoS_2, Nano Lett. **13**, 3626 (2013).

[80] D. J. Late, S. N. Shirodkar, U. V. Waghmare, V. P. Dravid, and C. N. R. Rao, *Thermal Expansion, Anharmonicity and Temperature-Dependent Raman Spectra of Single- and Few-Layer* $MoSe_2$ *and* WSe_2, ChemPhysChem **15**, 1592 (2014).

[81] S. Tongay, J. Zhou, C. Ataca, J. Liu, J. S. Kang, T. S. Matthews, L. You, J. Li, J. C. Grossman, and J. Wu, *Broad-Range Modulation of Light Emission in Two-Dimensional Semiconductors by Molecular Physisorption Gating*, Nano Lett. **13**, 2831 (2013).

[82] F. Cadiz, C. Robert, G. Wang, W. Kong, X. Fan, M. Blei, D. Lagarde, M. Gay, M. Manca, T. Taniguchi, K. Watanabe, T. Amand, X. Marie, P. Renucci, S. Tongay, and B. Urbaszek, *Ultra-low Power Threshold for Laser Induced Changes in Optical Properties of 2D Molybdenum Dichalcogenides*, 2D Mater. **3**, 045008 (2016).

[83] Y.-J. Yu, Y. Zhao, S. Ryu, L. E. Brus, K. S. Kim, and P. Kim, *Tuning the Graphene Work Function by Electric Field Effect*, Nano Lett. **9**, 3430 (2009).

[84] Y. Liang, S. Huang, R. Soklaski, and L. Yang, *Quasiparticle Band-Edge Energy and Band Offsets of Monolayer of Molybdenum and Tungsten Chalcogenides*, Appl. Phys. Lett. **103**, 042106 (2013).

[85] N. R. Wilson, P. V. Nguyen, K. Seyler, P. Rivera, A. J. Marsden, Z. P. L. Laker, G. C. Constantinescu, V. Kandyba, A. Barinov, N. D. M. Hine, X. Xu, and D. H. Cobden, *Determination of Band Offsets, Hybridization, and Exciton Binding in 2D Semiconductor Heterostructures*, Sci. Adv. **3**, e1601832 (2017).

[86] K. Kośmider and J. Fernández-Rossier, *Electronic Properties of the* MoS_2-WS_2 *Heterojunction*, Phys. Rev. B **87**, 075451 (2013).

[87] A. Kormányos, G. Burkard, M. Gmitra, J. Fabian, V. Zlyomi, N. D. Drummond, and V. Falko, $k \cdot p$ *Theory for Two-Dimensional Transition Metal Dichalcogenide Semiconductors*, 2D Mater. **2**, 022001 (2015).

[88] As a result, the relative magnitudes of the electron and hole flows, and the resulting steady-state E_F^{Gr} are not exclusively determined by Φ_{ph} (compare data in Fig. 5 and see Ref. [52], Fig. S13).

[89] M. M. Furchi, A. Pospischil, F. Libisch, J. Burgdrfer, and T. Mueller, *Photovoltaic Effect in an Electrically Tunable van der Waals Heterojunction*, Nano Lett. **14**, 4785 (2014).

[90] K. Kim, S. Larentis, B. Fallahazad, K. Lee, J. Xue, D. C. Dillen, C. M. Corbet, and E. Tutuc, *Band Alignment in* WSe_2*-Graphene Heterostructures*, ACS Nano **9**, 4527 (2015).

[91] P. Steinleitner, P. Merkl, P. Nagler, J. Mornhinweg, C. Schller, T. Korn, A. Chernikov, and R. Huber, *Direct Observation of Ultrafast Exciton Formation in a Monolayer of* WSe_2, Nano Lett. **17**, 1455 (2017).

[92] A. M. Jones, H. Yu, J. R. Schaibley, J. Yan, D. G. Mandrus, T. Taniguchi, K. Watanabe, H. Dery, W. Yao, and

X. Xu, *Excitonic Luminescence Upconversion in a Two-Dimensional Semiconductor*, Nat. Phys. **12**, 323 (2016).

[93] T. Chervy, S. Azzini, E. Lorchat, S. Wang, Y. Gorodetski, J. A. Hutchison, S. Berciaud, T. W. Ebbesen, and C. Genet, *Spin-Momentum Locked Polariton Transport in the Chiral Strong Coupling Regime*, arXiv:1701.07972.

[94] This conclusion is consistent with the fact that momentum conservation can be more easily fulfilled for an exciton than for a free charge carrier. Indeed, an exciton in the TMD can decay by transferring an electron or hole to a finite-momentum state graphene, leaving the other carrier in the TMD with the excess momentum [see Figs. 7(a) and 7(b)], whereas at room temperature, a free charge carrier near the band edges would need extra momentum provided by defect or phonon scattering.

[95] E. Malic, H. Appel, O. T. Hofmann, and A. Rubio, *Förster-Induced Energy Transfer in Functionalized Graphene*, J. Phys. Chem. C **118**, 9283 (2014).

[96] J. A. Schuller, S. Karaveli, T. Schiros, K. He, S. Yang, I. Kymissis, J. Shan, and R. Zia, *Orientation of Luminescent Excitons in Layered Nanomaterials*, Nat. Nanotechnol. **8**, 271 (2013).

[97] Let us note that the PL data in Figs. 1(f) and 2(e) have been recorded on a freshly made sample S_1 before recording the data in Figs. 2(c) and 2(d). Aging of the air-exposed $MoSe_2$ layer in S_1 is likely responsible for the fact that in Figs. 2(c) and 2(d), the PL intensity in $MoSe_2/SiO_2$ is slightly smaller than in decoupled $Gr/MoSe_2/SiO_2$, where graphene acts as an efficient passivating layer.

[98] A. Brenneis, L. Gaudreau, M. Seifert, H. Karl, M. S. Brandt, H. Huebl, J. A. Garrido, F. H. L. Koppens, and A. W. Holleitner, *Ultrafast Electronic Readout of Diamond Nitrogen-Vacancy Centres Coupled to Graphene*, Nat. Nanotechnol. **10**, 135 (2015).

[99] J. C. Johannsen, S. Ulstrup, F. Cilento, A. Crepaldi, M. Zacchigna, C. Cacho, I. C. Edmond Turcu, E. Springate, F. Fromm, C. Raidel, T. Seyller, F. Parmigiani, M. Grioni, and P. Hofmann, *Direct View of Hot Carrier Dynamics in Graphene*, Phys. Rev. Lett. **111**, 027403 (2013).

[100] I. Gierz, J. C. Petersen, M. Mitrano, C. Cacho, I. C. Edmond Turcu, E. Springate, A. Stöhr, A. Köhler, U. Starke, and A. Cavalleri, *Snapshots of Non-equilibrium Dirac Carrier Distributions in Graphene*, Nat. Mater. **12**, 1119 (2013).

[101] A. Castellanos-Gomez, M. Buscema, R. Molenaar, V. Singh, L. Janssen, H. S. J. van der Zant, and G. A. Steele, *Deterministic Transfer of Two-Dimensional Materials by All-Dry Viscoelastic Stamping*, 2D Mater. **1**, 011002 (2014).

Correction: The previously published Figures 2(c) and 2(d) contained axis label errors and were replaced.